Giant Anomalous Nernst Angle Induced by Berry Curvature in Layered Itinerant Ferromagnets

Yu-Ting Qian(钱玉婷)[1†], Jiu-Yun Zhang(张九匀)[2†], Xiang-Yu Bi(毕翔宇)[1†], Peng Chen(陈朋)[1], Hong-Zi Cao(曹洪兹)[1], Wei-Feng Xu(许玮峯)[1], Zhong-Yuan Liu(柳忠元)[3], Kun Zhai(翟昆)[3*], Hong-Tao Yuan(袁洪涛)[1*], and Jun-Wei Huang(黄俊伟)[1*]

[1]*National Laboratory of Solid State Microstructures, College of Engineering and Applied Sciences, and Collaborative Innovation Center of Advanced Microstructures, Nanjing University, Nanjing 210093, China*
[2]*School of Physics, Nanjing University, Nanjing 210093, China*
[3]*Center for High Pressure Science, State Key Laboratory of Metastable Materials Science and Technology, Yanshan University, Qinhuangdao 066004, China*

(Received 25 June 2025; accepted manuscript online 1 August 2025)

Berry curvature describes the intrinsic geometric property of electronic band structure, crucial for governing emergent transport phenomena. As a typical Berry-curvature-related property, the anomalous Nernst effect probes local Berry curvature near the Fermi surface, whereas the anomalous Hall effect integrates contributions across all occupied states. Thus, the anomalous Nernst effect is a superior probe for detecting subtle evolution of Berry curvature near the Fermi level; however, their relation remains elusive. Here, we demonstrate giant anomalous Nernst angles induced by Berry curvature in layered itinerant ferromagnets Fe_3GaTe_2 and Fe_5GeTe_2. Their maximum values (≈ 0.33 for Fe_3GaTe_2 and ≈ 0.41 for Fe_5GeTe_2) are one order of magnitude larger than those of traditional ferromagnets ($\theta_{AN}^{max} < 0.02$). Scaling analysis of anomalous Hall effect in these two systems further suggests these giant angles originate from intrinsic Berry curvature. These findings indicate Berry-curvature-dominated regimes, and establish these materials for high-performance spin-caloritronic devices.

DOI: 10.1088/0256-307X/42/9/090713 CSTR: 32039.14.0256-307X.42.9.090713

The Berry curvature, a geometric phase intrinsic to quantum wave functions, governs the interplay between the topological electronic states and magnetic order in correlated quantum materials.[1–3] The momentum-space Berry curvature has been reported to give rise to typical physical phenomena governed by spin–charge thermal coupling, such as the anomalous Hall effect (AHE) and anomalous Nernst effect (ANE),[4–8] in a variety of two-dimensional van der Waals magnetic materials.[9–11] Importantly, the AHE stems from the Brillouin-zone integral of the Berry curvature across all occupied states, whereas the ANE is extremely sensitive to its distribution near the Fermi level E_F.[12] This enables the ANE to resolve subtle Berry curvature evolution near the Fermi level and offers critical insights into topological electronic structures. Examples of ANE enhancement have been demonstrated through interfacial engineering and quantum critical scaling,[13–15] as well as the tunability of the AHE through strong spin-orbit coupling.[16–21] However, the connection of the Berry curvature with the AHE and ANE has not been experimentally demonstrated.

In this study, with electronic and thermal transport measurements, we demonstrated the influence of Berry curvature on AHE and ANE in layered itinerant ferromagnets, Fe_3GaTe_2 and Fe_5GeTe_2, reflected by their giant anomalous Nernst angles. The anomalous Nernst voltages in Fe_3GaTe_2 persist across the entire measured temperature range (below 310 K) with a maximum anomalous Nernst angle of $\theta_{AN}^{max} \approx 0.33$. In comparison, the anomalous Nernst voltages in Fe_5GeTe_2 are only detectable below 45 K, accompanied by a slightly larger $\theta_{AN}^{max} \approx 0.41$. These remarkable values, which exceed those of traditional ferromagnets by more than one order of magnitude,[22,23] are attributed to the effect of the Berry curvature near the Fermi level. Our results reveal the correlation between Berry curvature and anomalous Nernst response in layered materials and provide insights for designing spin-caloritronic devices based on two-dimensional ferromagnets.

Berry curvature plays a pivotal role in governing the AHE and ANE in ferromagnetic materials, with their physical origins in momentum-space topology. As schematically illustrated in Fig. 1(a), the Berry curvature, which accumulates near band crossings such as Weyl nodes or nodal lines, modulates the geometric phase of the electron wave functions and governs the transverse transport behavior.[24] When the Fermi level approaches these topologically sensitive regions, the contribution of Berry curvature to the electron states is maximized, leading to significantly enhanced AHE and ANE signals. Theoretically, the AHE arises from the global integration of the Berry curvature over all occupied states,[24] whereas the ANE is

†These authors contributed equally to this work.
*Corresponding authors. Email: kunzhai@ysu.edu.cn; htyuan@nju.edu.cn; junweihuang@nju.edu.cn
© 2025 Chinese Physical Society and IOP Publishing Ltd. All rights, including for text and data mining, AI training, and similar technologies, are reserved.

majorly determined by the local Berry curvature distribution near $E_{\rm F}$. Thus, the anomalous Hall conductivity σ_{xy} and anomalous transverse thermoelectric conductivity α_{xy} are expressed as follows:[5]

$$\sigma_{xy}(\varepsilon) = -\sum_{n} \frac{e^2}{\hbar} \int \mathrm{d}k \Omega_{n,z}(k) \Theta(\varepsilon - \varepsilon_{n,k}), \quad (1)$$

$$\alpha_{xy}(\mu, T) = \frac{1}{e} \int \mathrm{d}\varepsilon \frac{\partial f(\varepsilon)}{\partial \varepsilon} \frac{(\varepsilon - \mu)}{T} \sigma_{xy}(\varepsilon), \quad (2)$$

where $\varepsilon_{n,k}$ and $\Omega_{n,z}(k)$ are the band energy and Berry curvature of the n-band, respectively, $\sigma_{xy}(\varepsilon)$ is the anomalous Hall conductivity at zero temperature, $f(\varepsilon)$ is the Fermi–Dirac distribution function, e is the electron charge, T is the temperature, μ is the chemical potential, $\hbar$ is the reduced Planck's constant, and $\Theta(\varepsilon - \varepsilon_{n,k})$ is the step function. This distinct mechanism indicates that ANE is powerful probe for detecting subtle variations in the Berry curvature near the Fermi level.[25–28]

We intentionally chose two representative layered itinerant ferromagnets Fe_3GaTe_2 and Fe_5GeTe_2 as targeted systems for the following three reasons. First, the breaking of time-reversal symmetry by long-range ferromagnetic order in both materials facilitates nonzero net Berry curvature accumulation in momentum space, which allows the observations of AHE and ANE. Second, the strong spin–orbit coupling owing to the hybridization of the Te-5p and Fe-3d orbitals induces spin-polarized Berry curvature distributions, providing an ideal platform for exploring transverse charge/thermal transport phenomena.[29–35] Third, out-of-plane magnetization can modify the band dispersion via exchange interactions and redistributes the Berry curvature to favor transverse thermal gradients in the ANE. Interestingly, Fe_3GaTe_2 and Fe_5GeTe_2 exhibit distinct magnetic anisotropy characteristics: Fe_3GaTe_2 exhibits pronounced perpendicular magnetic anisotropy stabilized by strong spin–orbit coupling, whereas Fe_5GeTe_2 displays temperature-tunable anisotropy arising from its weak interlayer exchange coupling. The above characteristics of these two materials provide a unique platform for comparatively investigating the Berry curvature-driven AHE and ANE in materials with a distinctive magnetic anisotropy.

To understand the temperature and magnetic field dependencies of the AHE and ANE, we performed electronic

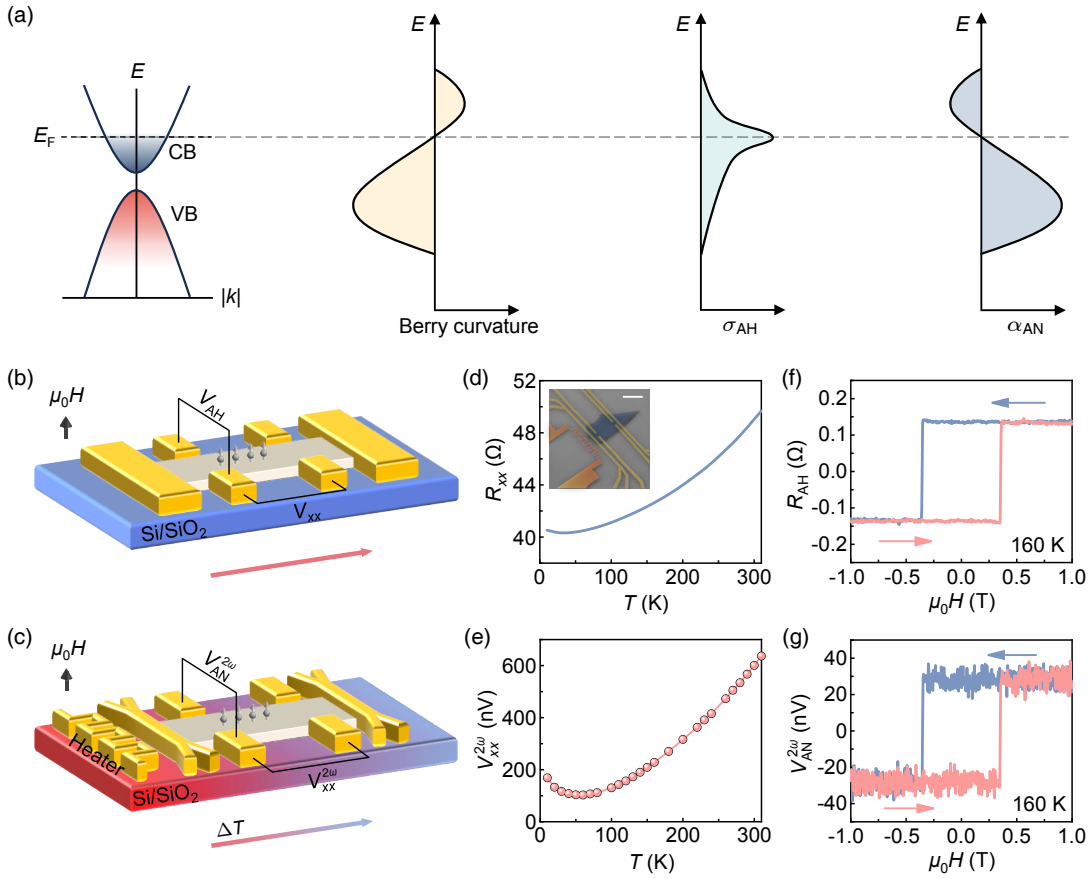

Fig. 1. Berry curvature-induced AHE and ANE. (a) Schematic illustration of the relationship between band structure, AHE, ANE, and Berry curvature in ferromagnetic materials, where CB represents the conduction band and VB represents the valence band. (b) and (c) Measurement principles and device schematics for AHE and ANE in ferromagnetic materials. (d)–(g) Fundamental electrical and thermal transport data of Fe_3GaTe_2: (d) Temperature dependence of longitudinal resistance (R_{xx}), with the inset showing the scanning electron microscopy image of the device, where the length of the white solid line is 20 μm; (e) Temperature dependence of longitudinal Seebeck voltage ($V_{xx}^{2\omega}$); (f) AHE signal obtained from anomalous Hall resistance ($R_{\rm AH}$) measurements under varying out-of-plane magnetic field at 160 K; (g) ANE signal obtained from anomalous Nernst voltage ($V_{\rm AN}^{2\omega}$) measurements under varying out-of-plane magnetic field at 160 K.

and thermal transport measurements under varying temperature and magnetic field ($\mu_0 H$) by using the geometries shown in Figs. 1(b) and 1(c), respectively. For the electronic transport measurements, a standard Hall bar geometry was employed to simultaneously measure the longitudinal resistance (R_{xx}) and anomalous Hall resistance ($R_{\rm AH}$) by applying an in-plane electrical current [Fig. 1(b)]. For the thermal transport measurements, the geometry was modified by adding a local heater and thermocouples to apply and detect the temperature gradients (ΔT) across the flake [Fig. 1(c), additional details are provided in Fig. S1 of the Supplementary Materials (SM)]. This geometry allows the simultaneous detection of the longitudinal Seebeck voltage ($V_{xx}^{2\omega}$) and transverse Nernst voltage ($V_{\rm AN}^{2\omega}$) driven by a steady ΔT. In our experiments, the electronic and thermal transport measurements were carried out by applying a current and ΔT, respectively, in a single device with the geometry shown in the inset of Fig. 1(d). Figures 1(d) and 1(e) presents the temperature-dependent R_{xx} and $V_{xx}^{2\omega}$ of Fe_3GaTe_2 measured in the same flake with a thickness of 80 nm. The R_{xx}–T curve decreases monotonically as the temperature decreases and exhibits a slight upward trend below approximately 50 K. This is consistent with the typical metallic behavior of Fe_3GaTe_2 reported previously.[33] In comparison, the trend of the $V_{xx}^{2\omega}$–T curve in Fig. 1(e) is consistent with that of the R_{xx}–T curve in Fig. 1(d).

We further compared the hysteresis loops of magnetic-field-dependent $R_{\rm AH}$ [Fig. 1(f)] and $V_{\rm AN}^{2\omega}$ [Fig. 1(g)] at 160 K. The hysteresis loops of both $R_{\rm AH}$–$\mu_0 H$ and $V_{\rm AN}^{2\omega}$–$\mu_0 H$ exhibit similar rectangular shapes and a consistent coercive field with a value of approximately 0.35 T, suggesting robust ferromagnetic ordering and strong out-of-plane magnetic anisotropy in Fe_3GaTe_2.[33] The consistency between the AHE and ANE responses highlights their shared origin in the Berry curvature, because the geometric phase modulation of electron states simultaneously influences both electrical and thermal transverse transport.[3,36] The robust ferromagnetic ordering and strong perpendicular magnetic anisotropy establish Fe_3GaTe_2 as a promising material for exploring the Berry curvature-mediated spin–charge thermal coupling phenomena in low-dimensional ferromagnets.

To further study the evolution of the AHE and ANE hysteresis loops with temperature, we performed electronic and thermal transport measurements of Fe_3GaTe_2 by sweeping the external magnetic fields over a broad temperature range of 10–310 K [Figs. 2(a) and 2(b), and Figs. S2 and S3 in the SM]. In Fig. 2(a), the AHE hysteresis loop at 10 K shows a rectangular shape with a coercive field ($\mu_0 H_{\rm C}$) of approximately 0.9 T, indicating a hard-ferromagnetic nature.[7] The $\mu_0 H_{\rm C}$ value gradually decreases with increasing temperatures [Fig. S4(c) of the SM], and the hysteresis loops evolve from rectangular shapes at low temperatures to "narrow-waisted" profiles at 310 K. On the one hand, the observed morphological evolution of the hysteresis loops originates from the temperature-dependent magnetic domain dynamics: the single-domain state dominates magnetization reversal at low temperatures, whereas topological magnetic multi-domain structures (e.g., vortices or skyrmions) emerge at high temperatures, resulting in slight jumps in $R_{\rm AH}$ near 0 T.[37] On the other hand, the magnetization reversal process in the AHE for Fe_3GaTe_2 is associated with the Berry curvature of occupied electronic states in momentum space (discussed in detail later), which is consistent with those in other two-dimensional ferromagnetic materials such as Fe_3GeTe_2 and Cr_7Te_8.[6,38,39]

Analogous to the AHE characteristics shown in Fig. 2(a), the shapes of the ANE hysteresis loops exhibited a similar temperature-dependent evolution [Fig. 2(b)]. The $\mu_0 H_{\rm C}$–T data extracted from the ANE curves were consistent with that obtained from the AHE curves [Fig. S4(c) of the SM]. However, the amplitude of $V_{\rm AN}^{2\omega}$ exhibited a distinct nonmonotonic temperature response: it increased from 10 K to 180 K before decaying at elevated temperatures, which sharply contrasted with the monotonic AHE trend [Fig. S4(d) of the SM]. This divergence from the AHE behavior highlights the sensitivity of the ANE to the dynamic redistribution of the Berry curvature near $E_{\rm F}$. To understand this unconventional behavior, we measured the longitudinal (S_{xx}) and transverse (S_{xy}) Seebeck coefficients [Figs. 2(c) and 2(d)]. While S_{xx} increased monotonically with increasing temperature, S_{xy} shows a peak near 180 K. Correspondingly, the temperature-dependent longitudinal ($\rm PF_{Seebeck}$) and transverse ($\rm PF_{Nernst}$) power factors exhibited a similar divergence [Fig. S8 of the SM]. The saturated anomalous Hall resistance ($R_{\rm AH}$) extracted from the AHE loops [Fig. 2(e)] decreased monotonically with increasing temperature, following the Bloch law: $R_{\rm AH}(T) = R_{\rm AH}(0)(1 - T/T_{\rm C})^{\beta}$,[40] and yielded a Curie temperature $T_{\rm C}$ of approximately 327 K. This result is consistent with the itinerant ferromagnetic nature of Fe_3GaTe_2, in which thermal excitation progressively disrupts the long-range magnetic order.

Since the AHE can be attributed to different origins, including the Berry curvature, skew scattering, and side jump, scaling analysis is required to separate the contribution of the Berry curvature from those of others. Scaling analysis is a powerful method that effectively distinguishes between various contributions in AHE, and displays their different origins owing to different scaling relations between the anomalous Hall resistivity (ρ_{xy}) and longitudinal resistivity (ρ_{xx}): (i) intrinsic Berry curvature region ($\rho_{xy} \propto \rho_{xx}^2$ and the anomalous Hall conductivity σ_{xy} is constant), (ii) skew-scattering region ($\rho_{xy} \propto \rho_{xx}$ and $\sigma_{xy} \propto \sigma_{xx}$, where σ_{xx} is the longitudinal conductivity), and (iii) side-jump region between them.[24] Therefore, we present the scaling relation of the resistivity as $\rho_{xy}/\rho_{xx} = a + b\rho_{xx}$ (described in Note 9 of the SM).[24] The plot of ρ_{xy}/ρ_{xx} versus ρ_{xx} [Fig. 2(f)] indicated that Fe_3GaTe_2 follows the relation of $\rho_{xy} \propto \rho_{xx}^2$ across the whole measured temperature regime of 10–310 K, confirming the dominance of Berry curvature in the AHE.[41] While the AHE originates from the integration of the Berry curvature across all the occupied bands, only the bands near the Fermi surface contribute

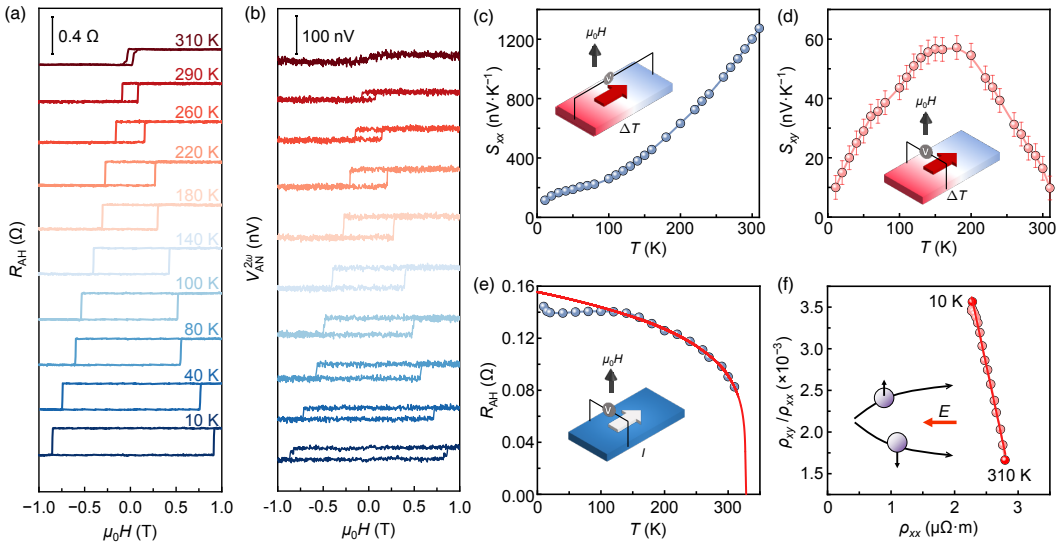

Fig. 2. Berry curvature-dominated AHE and ANE across the full temperature range in Fe_3GaTe_2. (a) AHE signals obtained from R_{AH} measurements under out-of-plane magnetic field at various temperatures, with scale bar indicated in the top-left corner. (b) ANE signals obtained from $V_{AN}^{2\omega}$ measurements under out-of-plane magnetic field at different temperatures, with scale bar shown in the top-left corner (curves with identical colors correspond to the same temperatures as in panel (a). (c) and (d) Temperature dependence of S_{xx} and S_{xy}, with inset showing the measurement scheme. (e) Temperature evolution of R_{AH}, with inset depicting the measurement geometry. The red curve represents a fit based on Bloch's law, yielding a Curie temperature T_C of ∼327 K. (f) Scaling analysis of AHE mechanisms. The inset shows a schematic of Berry curvature, indicating that both AHE and ANE in Fe_3GaTe_2 from 10–310 K are dominated by Berry curvature, as evidenced by the excellent agreement with scaling analysis.

to the ANE. The similarities between the AHE and ANE in Fe_3GaTe_2 suggest that its Berry curvature is maintained over the entire temperature range, whereas their differences reflect the high sensitivity to changes in bands near the Fermi surface in the ANE. Therefore, as a sensitive probe of the Fermi surface, ANE measurements could effectively demonstrate the evolution of the Berry curvature in ferromagnetic materials.

To check if there will be any difference in Berry-curvature induced phenomena due to distinctive magnetic anisotropy and electronic structure, we performed AHE and ANE measurements by varying the magnetic field and temperature in Fe_5GeTe_2. As shown in Fig. 3(a), we plotted the anomalous Hall resistance R_{AH} (red balls) and the anomalous Nernst voltage $V_{AN}^{2\omega}$ (blue balls) as a function of the temperature (details in Fig. S5 of the SM). In addition, the plot shows a fit for R_{AH} above 100 K (blue solid line) by Bloch's law, which reflects a Curie temperature of 295 K (details in Fig. S7 of the SM). Interestingly, R_{AH} peaks near 100 K before sharply decreasing as the temperature decreases, deviating from conventional magnetization saturation. This behavior correlates with magnetic ordering in the Fe_1 sublattice and a concurrent electronic Lifshitz transition at $T_M \approx 100$ K,[42,43] as evidenced by nonmonotonic coercive field evolution in the AHE (Fig. S6 of the SM). In sharp contrast, the anomalous Nernst voltage $V_{AN}^{2\omega}$ decayed rapidly below 45 K and disappeared completely as temperature increased [Fig. 3(a)].

Moreover, we observed that the coercivity H_C in the ANE dropped abruptly to zero when $T > 45$ K (Fig. S6 of the SM), indicating that the suppression of the Berry curvature contributed to the ANE. Furthermore, the Seebeck coefficient S_{xx} decreased sharply below 45 K and increased persistently at higher temperatures [Fig. 3(b)]. In contrast, the plot of the Nernst coefficients S_{xy} versus temperature [Fig. 3(c)] decayed rapidly with temperatures below 45 K and vanished completely when the temperature increased, exhibiting a temperature dependence similar to that of the anomalous Nernst voltage $V_{AN}^{2\omega}$. The contrasting behaviors (decrease in S_{xy}, as opposed to the decrease and subsequent increase in S_{xx}) indicate ANE regulation via competition between Berry curvature and thermal excitation. Both the coefficients demonstrated critical transitions near 45 K. In addition, all the devices exhibited abrupt attenuation of longitudinal (S_{xx}, $PF_{Seebeck}$, $V_{xx}^{2\omega}$) and transverse (S_{xy}, PF_{Nernst}, $V_{AN}^{2\omega}$) signals below the critical temperature (Figs. S6 and S9 of the SM). This universal suppression confirms the existence of a characteristic transition temperature that governs ANE signal collapse.

To probe the origin of the sharp contrast between the AHE and ANE behaviors at low temperatures in Fe_5GeTe_2, we performed a scaling analysis based on the R_{AH}–T data. In Fig. 3(d), ρ_{xy}/ρ_{xx} is plotted as a function of ρ_{xx} (red balls), where the slope (γ) and intercept represents the contribution of intrinsic Berry curvature and skew scattering, respectively. For $T > 70$ K, the flat slope ($\gamma \approx 0$, red dashed line) indicates that AHE is dominated by skew scattering. Below 45 K, γ deviates from zero (blue dashed line), revealing the increasing contribution of Berry curvature. Therefore, we estimated the components of the anomalous Hall conductivity that originated from the Berry curvature and skew scattering [Fig. 3(e)]. Upon separating the intrinsic (Berry curvature) and extrinsic (skew scattering) contributions, the Berry curvature was significant only below the critical temperature $T_B \approx 45$ K. Above T_B, its contribution diminished to within experimental

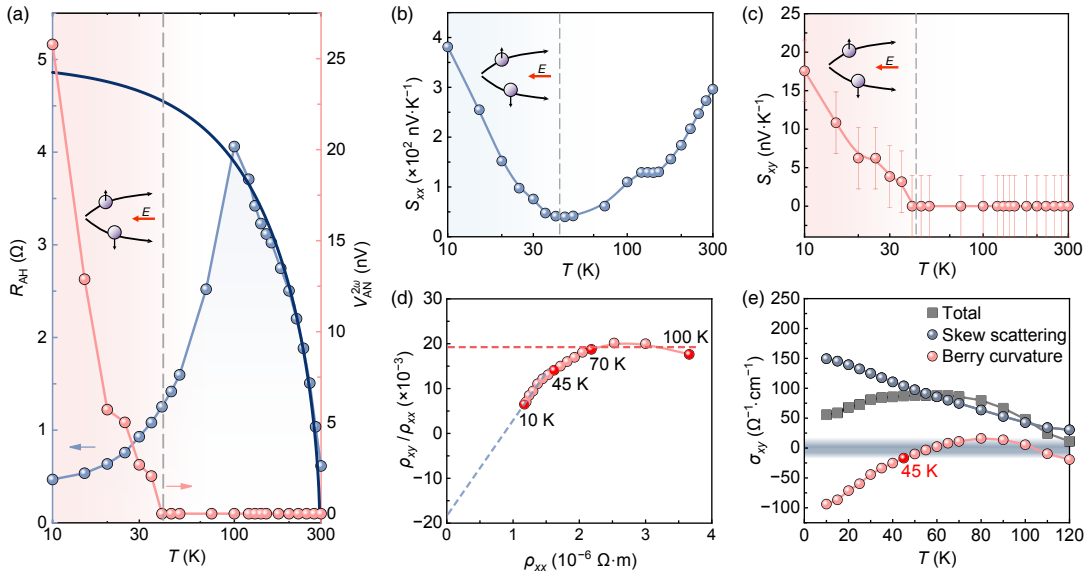

Fig. 3. Berry curvature-dominated AHE and ANE only in the low-temperature regime of Fe_5GeTe_2. (a) Temperature dependence of AHE and ANE signals in Fe_5GeTe_2. Red circles represent $V_{AN}^{2\omega}$, blue circles denote R_{AH}, and the dark blue curve shows a fit based on Bloch's law, yielding a T_C of ∼295 K. The dashed line in the figure demarcates the critical transition where the $V_{AN}^{2\omega}$ vanishes, corresponding to a temperature of approximately 45 K. (b) Temperature evolution of S_{xx}. The dashed line in the figure marks the critical point at which the S_{xx} switches from decreasing to increasing, occurring at approximately 45 K. (c) Temperature dependence of S_{xy}, with pale red lines indicating error bars. The dashed line in the figure demarcates the critical transition where the S_{xy} vanishes, corresponding to a temperature of approximately 45 K. (d) Scaling analysis of AHE mechanisms. The slope represents the intrinsic Berry curvature contribution to AHE, while the intercept corresponds to the extrinsic skew-scattering contribution. The data points marked in red represent the special temperatures we want to highlight. The red dashed line (slope $\gamma \approx 0$) indicates skew-scattering dominance at $T > 70$ K, while the blue dashed line ($\gamma \neq 0$) shows increasing Berry curvature contribution below 45 K. (e) Separation of Berry curvature and skew-scattering contributions to AHE with their respective temperature dependences. Blue circles indicate the Berry curvature contribution, red circles represent the skew-scattering contribution, and black squares denote the total anomalous Hall conductivity.

error, which was consistent with the disappearance of both $V_{AN}^{2\omega}$ and S_{xy} signals. The critical temperature T_B above which the Berry curvature contribution became negligible closely matches the transition point, as observed in the ANE measurements. The temperature evolution of the Berry curvature enables the ANE to detect this critical transition at T_B, demonstrating its unique capability to probe additional topological properties. Consequently, it provides new insights into Berry curvature dynamics in layered itinerant ferromagnets.

To establish the physical mechanism of AHE in layered itinerant ferromagnets, we plotted the anomalous Hall conductivity σ_{xy} versus the longitudinal conductivity σ_{xx} for various classical ferromagnets [Fig. 4(a)]. The functional relationship between Hall conductivity (σ_{xy}) and longitudinal conductivity (σ_{xx}) revealed distinct regimes: at high σ_{xx} ($>3\times10^5\,\Omega^{-1}\cdot\mathrm{cm}^{-1}$), skew scattering dominated owing to asymmetric momentum relaxation; intermediate σ_{xx} (3×10^3–$3\times10^5\,\Omega^{-1}\cdot\mathrm{cm}^{-1}$) reflected intrinsic Berry curvature contributions from global band integration; and low σ_{xx} ($<3\times10^3\,\Omega^{-1}\cdot\mathrm{cm}^{-1}$) exhibited side-jump dominance via scattering-induced transverse displacements. Fe_3GaTe_2 maintained its intrinsic behavior across all temperatures, which was consistent with its global Berry curvature dominance. In contrast, Fe_5GeTe_2 transitions from intrinsic Berry curvature dominance at low temperatures ($T < 45$ K) to side-jump dominance at high temperatures ($T > 90$ K), which corroborates the suppression of ANE above $T_B \approx 45$ K. These results highlight the critical role of Berry curvature in determining the transport regimes in layered ferromagnets.

To realize the applications in thermoelectric Hall devices of Fe_3GaTe_2 and Fe_5GeTe_2, we plotted the anomalous Nernst angle θ_{AN} as a function of the temperature for various classical ferromagnets in Fig. 4(b). One can see that Fe_3GaTe_2 achieves $\theta_{AN}^{max} \approx 0.33$ at 80 K, while Fe_5GeTe_2 reaches $\theta_{AN}^{max} \approx 0.41$ at 35 K, which exceed those of conventional ferromagnets ($\theta_{AN}^{max} < 0.02$) by more than one order of magnitude.[22,23,44,45] These results align with topological materials such as Cr_5Te_8 ($\theta_{AN}^{max} \approx 0.37$) and Co_2MnGa ($\theta_{AN}^{max} \approx 0.24$), which exhibit strong Berry curvature signatures from Weyl nodes or topological spin textures.[2,4,5,15,46–50] The superior performance of Fe_5GeTe_2 arises from the localized Berry curvature enhancement near E_F at low temperatures, whereas the broad operational temperature range (10–180 K) of Fe_3GaTe_2 stems from its robust Berry curvature stability. Notably, high θ_{AN} materials share common features, namely, topological band structures with Berry curvature singularities near E_F. Furthermore, we compared the temperature dependence of anomalous Hall angles (θ_{AH}) for Fe_3GaTe_2 and Fe_5GeTe_2 with various classical ferromagnetic materials (Fig. S12 of the SM). Fe_5GeTe_2 exhibited nonmonotonic θ_{AH} with a peak of ∼0.05 at low

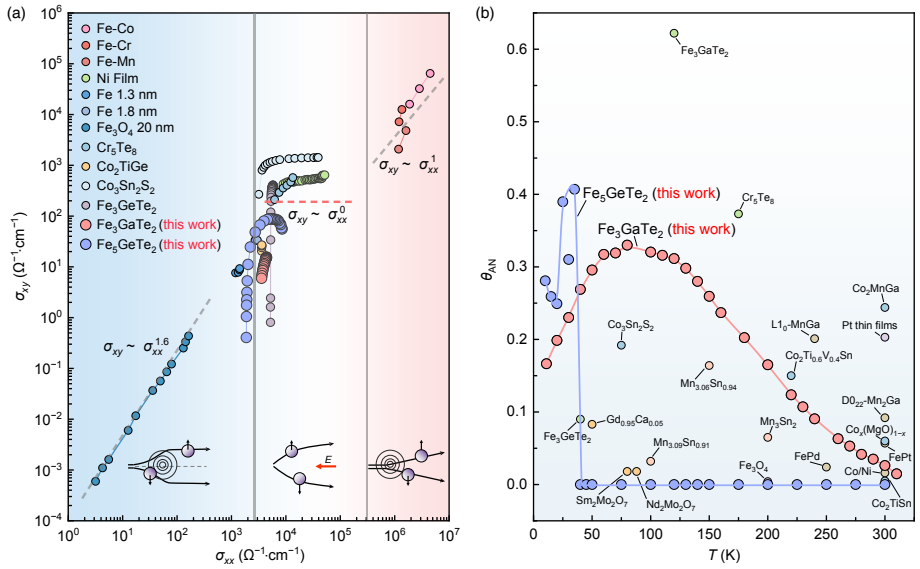

Fig. 4. Giant anomalous Nernst angle induced by Berry curvature in itinerant ferromagnets Fe_3GaTe_2 and Fe_5GeTe_2. (a) Analysis of AHE mechanisms in magnetic materials as a function of resistivity.[11,13,19,49,51–56] The scaling relationship between σ_{xy} and σ_{xx} reveals three distinct regimes: (i) side-jump regime ($\sigma_{xy} \propto \sigma_{xx}^{1.6}$); (ii) intrinsic Berry curvature regime ($\sigma_{xy} \approx$ constant), and (iii) skew-scattering regime ($\sigma_{xy} \propto \sigma_{xx}$). (b) Survey of θ_{AN} at different temperatures in magnetic materials.[7,11,15,22,23,41,42,46,47,49,57–59]

temperatures, whereas Fe_3GaTe_2 monotonically decreased to $\theta_{AH}^{max} \approx 0.007$. Despite the lower θ_{AH}, Fe_3GaTe_2 exhibited stable θ_{AH} across temperatures, thereby highlighting the unique advantages of ANE over AHE in probing topological transport. These findings validate the universality of the Berry curvature-induced ANE in layered ferromagnets and facilitate the optimization of thermoelectric devices by engineering topological band structures in low-dimensional systems.

In summary, we investigated the electronic and thermoelectric transport behaviors of layered itinerant ferromagnets Fe_3GaTe_2 and Fe_5GeTe_2, revealing the role of the Berry curvature in governing the AHE and ANE. Our findings highlight the critical role of Berry curvature in topological transport and establish the ANE as a sensitive probe for Berry curvature near E_F. The giant θ_{AN} values in both materials surpassed those of traditional ferromagnets by one order of magnitude, demonstrating their potential applications in thermoelectric Hall devices. The observed correlation between θ_{AN} and AHE (ANE) in Fe_3GaTe_2, Fe_5GeTe_2, and other high-performance systems (e.g., Cr_5Te_8 and Co_2MnGa) provides a universal approach for optimizing thermoelectric performance through Berry curvature engineering. This study advances the understanding of topological spin–heat coupling and paves the way for novel devices that integrate topological and thermoelectric functionalities in low-dimensional materials.

Acknowledgements. This work was supported by the National Key Research and Development Program of China (Grant Nos. 2024YFA1408104, 2021YFA1202901, and 2022YFA1204001), the National Natural Science Foundation of China (Grant Nos. 92365203, U24A6002, 52302180, and U21A2086), the Natural Science Foundation of Jiangsu Province (Grant No. BK20243011), and the Hebei Natural Science Foundation (Grant No. E2023203002).

References

[1] Pan Y, Le C C, He B, Watzman S J, Yao M Y, Gooth J, Heremans J P, Sun Y, and Felser C 2021 *Nat. Mater.* **21** 203

[2] Sakai A, Minami S, Koretsune T, Chen T S, Higo T, Wang Y M, Nomoto T, Hirayama M, Miwa S, Nishio-Hamane D, Ishii F, Arita R, and Nakatsuji S 2020 *Nature* **581** 53

[3] Xiao D, Chang M C, and Niu Q 2010 *Rev. Mod. Phys.* **82** 1959

[4] Gupta S, Emmanuel O O, Ozbek Y, Xu M Y, Xie W W, Zhang P P, and Ke X L 2025 *Mater. Today Phys.* **50** 101627

[5] Li M H, Pi H Q, Zhao Y C, Lin T, Zhang Q H, Hu X Z, Xiong C M, Qiu Z Y, Wang L C, Zhang Y, Cai J W, Liu W M, Sun J R, Hu F X, Gu L, Weng H M, Wu Q S, Wang S G, Chen Y Z, and Shen B G 2023 *Adv. Mater.* **35** 2301339

[6] Meng K, Li Z Y, Gao Z S, Bi X Y, Chen P, Qin F, Qiu C Y, Xu L Y, Huang J W, Wu J X, Luo F, and Yuan H T 2024 *InfoMat* **6** e12524

[7] Wang M J, Lei B, Zhu K J, Deng Y Z, Tian M L, Xiang Z J, Wu T, and Chen X H 2024 *npj 2D Mater. Appl.* **8** 22

[8] Xu J S, Phelan W A, and Chien C L 2019 *Nano Lett.* **19** 8250

[9] Belopolski I, Watanabe R, Sato Y, Yoshimi R, Kawamura M, Nagahama S, Zhao Y L, Shao S, Jin Y J, Kato Y, Okamura Y, Zhang X X, Fujishiro Y, Takahashi Y, Hirschberger M, TsukazakiA, Takahashi K S, Chiu C K, Chang G Q, Kawasaki M, Nagaosa N, and Tokura Y 2025 *Nature* **637** 1078

[10] Leiva L, Granville S, Zhang Y, Dushenko S, Shigematsu E, Shinjo T, Ohshima R, Ando Y, and Shiraishi M 2021 *Phys. Rev. B* **103** L041114

[11] Cheng E J, Yan L M, Shi X B, Lou R, Fedorov A, Behnami M, Yuan J, Yang P T, Wang B S, Cheng J G, Xu Y J,

Xu Y, Xia W, Pavlovskii N, Peets D C, Zhao W W, Wan Y M, Burkhardt U, Guo Y F, Li S Y, Felser C, Yang W G, and Büchner B 2024 *Nat. Commun.* **15** 1467
[12] Noky J, Zhang Y, Gooth J, Felser C, and Sun Y 2020 *npjComput. Mater.* **6** 77
[13] Miyasato T, Abe N, Fujii T, Asamitsu A, Onoda S, Onose Y, Nagaosa N, and Tokura Y 2007 *Phys. Rev. Lett.* **99** 086602
[14] Pu Y, Chiba D, Matsukura F, Ohno H, and Shi J 2008 *Phys. Rev. Lett.* **101** 117208
[15] Sakai A, Mizuta Y, Nugroho A, Sihombing R, Koretsune T, Suzuki M, Takemori N, Ishii R, Nishio-Hamane D, Arita R, Goswami P, and Nakatsuji S 2018 *Nat. Phys.* **14** 1119
[16] Deng Y J, Yu Y J, Song Y C, Zhang J Z, Wang N Z, Sun Z Y, Yi Y F, Wu Y Z, Wu S W, Zhu J Y, Wang J, Chen X H, and Zhang Y B 2018 *Nature* **563** 94
[17] Gong C, Li L, Li Z L, Ji H W, Stern A, Xia Y, Cao T, Bao W, Wang C Z, Wang Y, Qiu Z Q, Cava R J, Louie S G, Xia J, and Zhang X 2017 *Nature* **546** 265
[18] Tan C, Lee J, Jung S G, Park T, Albarakati S, Partridge J, Field M R, McCulloch D G, Wang L, and Lee C 2018 *Nat. Commun.* **9** 1554
[19] Tang B J, Wang X W, Han M J, Xu X D, Zhang Z W, Zhu C, Cao X, Yang Y M, Fu Q D, Yang J Q, Li X J, Gao W B, Zhou J D, Lin J H, and Liu Z 2022 *Nat. Electron.* **5** 224
[20] Wang H Y, Liu Y J, Wu P C, Hou W J, Jiang Y H, Li X H, Pandey C, Chen D D, Yang Q, Wang H T, Wei D H, Lei N, Kang W, Wen L G, Nie T X, Zhao W S, and Wang K L 2020 *ACS Nano* **14** 10045
[21] Wang H T, Lu H C, Guo Z X, Li A, Wu P C, Li J, Xie W R, Sun Z M, Li P, Damas H, Friedel A M, Migot S, Ghanbaja J, Moreau L, Fagot-Revurat Y, Petit-Watelot S, Hauet T, Robertson J, Mangin S, Zhao W S, and Nie T X 2023 *Nat. Commun.* **14** 2483
[22] Chuang T C, Su P L, Wu P H, and Huang S Y 2017 *Phys. Rev. B* **96** 174406
[23] Ramos R, Aguirre M H, Anadón A, Blasco J, Lucas I, Uchida K, Algarabel P A, Morellón L, Saitoh E, and Ibarra M R 2014 *Phys. Rev. B* **90** 054422
[24] Nagaosa N, Sinova J, Onoda S, MacDonald A H, and Ong N P 2010 *Rev. Mod. Phys.* **82** 1539
[25] Grauby S, Ben Amor A, Hallais G, Vincent L, and Dilhaire S 2021 *Nanomaterials* **11** 1199
[26] Liu S, Chen M Z, Fu C G, and Zhu T J 2023 *Adv. Phys. Res.* **2** 2300015
[27] Otani Y, Shiraishi M, Oiwa A, Saitoh E, and Murakami S 2017 *Nat. Phys.* **13** 829
[28] Xu Y F, Zhou X F, and Jin G J 2016 *Appl. Phys. Lett.* **108** 203104
[29] Lee J E, Yan S H, Oh S, Hwang J, Denlinger J D, Hwang C, Lei H C, Mo S K, Park S Y, and Ryu H 2023 *Nano Lett.* **23** 11526
[30] Li Z X, Xia W, Su H, Yu Z H, Fu Y P, Chen L M, Wang X, Yu N, Zou Z Q, and Guo Y F 2020 *Sci. Rep.* **10** 15345
[31] May A F, Ovchinnikov D, Zheng Q, Hermann R, Calder S, Huang B, Fei Z Y, Liu Y H, Xu X D, and McGuire M A 2019 *ACS Nano* **13** 4436
[32] Ruiz A M, Esteras D L, López-Alcalá D, and Baldoví J J 2024 *Nano Lett.* **24** 7886
[33] Zhang G J, Guo F, Wu H, Wen X K, Yang L, Jin W, Zhang W F, and Chang H X 2022 *Nat. Commun.* **13** 5067
[34] Zhang H R, Chen R, Zhai K, Chen X, Caretta L, Huang X X, Chopdekar R V, Cao J H, Sun J R, Yao J, Birgeneau R, and Ramesh R 2020 *Phys. Rev. B* **102** 064417
[35] Cho W, Kang Y G, Cha J, Lee D H D, Kiem D H, Oh J, Joo Y, Yer S, Kim D, Park J, Kim C, Yang Y, Kim Y, Han M J, and Yang H 2024 *Adv. Mater.* **36** 2402040
[36] Xiao D, Yao Y G, Fang Z, and Niu Q 2006 *Phys. Rev. Lett.* **97** 026603
[37] Liu S H, Hu S J, Cui X M, and Kimura T 2023 *Adv. Mater.* **36** 2309776
[38] Meng K, Li Z Y, Shen Y C, Bi X Y, Rao J H, Qian Y T, Gao Z S, Chen P, Qiu C Y, Qin F, Wu J X, Luo F, Huang J W, and Yuan H T 2024 *Chin. Phys. Lett.* **41** 097501
[39] Wu Y Y, Francisco B, Chen Z J, Wang W, Zhang Y, Wan C H, Han X F, Chi H, Hou Y S, Lodesani A, Yin G, Liu K, Cui Y T, Wang K L, and Moodera J S 2022 *Adv. Mater.* **34** 2110583
[40] Liu E K, Sun Y, Kumar N, Muechler L, Sun A L, Jiao L, Yang S Y, Liu D F, Liang A J, Xu Q N, Kroder J, Süß V, Borrmann H, Shekhar C, Wang Z S, Xi C Y, Wang W H, Schnelle W, Wirth S, Chen Y L, Goennenwein S, and Felser C 2018 *Nat. Phys.* **14** 1125
[41] Siddiquee H, Broyles C, Kotta E, Liu S Z, Peng S Y, Kong T, Kang B, Zhu Q, Lee Y, Ke L Q, Weng H M, Denlinger J D, Wray L A, and Ran S 2023 *Nat. Commun.* **14** 527
[42] Deng Y Z, Xiang Z J, Lei B, Zhu K J, Mu H M, Zhuo W Z, Hua X Y, Wang M J, Wang Z F, Wang G P, Tian M L, and Chen X H 2022 *Nano Lett.* **22** 9839
[43] Tang M, Huang J W, Qin F, Zhai K, Ideue T, Li Z Y, Meng F H, Nie A M, Wu L L, Bi X Y, Zhang C R, Zhou L, Chen P, Qiu C Y, Tang P Z, Zhang H J, Wan X G, Wang L, Liu Z Y, Tian Y J, Iwasa Y, and Yuan H T 2023 *Nat. Electron.* **6** 28
[44] Hanasaki N, Sano K, Onose Y, Ohtsuka T, Iguchi S, Kézsmárki I, Miyasaka S, Onoda S, Nagaosa N, and Tokura Y 2008 *Phys. Rev. Lett.* **100** 106601
[45] Hasegawa K, Mizuguchi M, Sakuraba Y, Kamada T, Kojima T, Kubota T, Mizukami S, Miyazaki T, and Takanashi K 2015 *Appl. Phys. Lett.* **106** 252405
[46] Guin S N, Manna K, Noky J, Watzman S J, Fu C G, Kumar N, Schnelle W, Shekhar C, Sun Y, and Gooth J 2019 *NPG Asia Mater.* **11** 16
[47] Guin S N, Vir P, Zhang Y, Kumar N, Watzman S J, Fu C G, Liu E K, Manna K, Schnelle W, Gooth J, Shekhar C, Sun Y, and Felser C 2019 *Adv. Mater.* **31** 1806622
[48] Reichlova H, Schlitz R, Beckert S, Swekis P, Markou A, Chen Y C, Kriegner D, Fabretti S, Park G H, Niemann A, Sudheendra S, Thomas A, Nielsch K, Felser C, and Goennenwein S T B 2018 *Appl. Phys. Lett.* **113** 212405
[49] Yang H Y, You W, Wang J L, Huang J W, Xi C Y, Xu X F, Cao C, Tian M L, Xu Z A, Dai J, and Li Y 2020 *Phys. Rev. Mater.* **4** 024202
[50] Zhou W N, Yamamoto K, Miura A, Iguchi R, Miura Y, Uchida K I, and Sakuraba Y 2021 *Nat. Mater.* **20** 463
[51] Dulal R P, Dahal B R, Forbes A, Bhattarai N, Pegg I L, and Philip J 2019 *Sci. Rep.* **9** 3342
[52] Fernández-Pacheco A, De Teresa J M, Orna J, Morellon L, Algarabel P A, Pardo J A, and Ibarra M R 2008 *Phys. Rev. B* **77** 100403
[53] Majumdar A K and Berger L 1973 *Phys. Rev. B* **7** 4203
[54] Sangiao S, Morellon L, Simon G, De Teresa J M, Pardo J A, Arbiol J, and Ibarra M R 2009 *Phys. Rev. B* **79** 014431
[55] Shiomi Y, Onose Y, and Tokura Y 2009 *Phys. Rev. B* **79** 100404
[56] Yang S Y, Noky J, Gayles J, Dejene F K, Sun Y, Dörr M, Skourski Y, Felser C, Ali M N, Liu E K, and Parkin S S P 2020 *Nano Lett.* **20** 7860
[57] Bai J L, Dong Q X, Ruan B B, Zhang L B, Liu Q Y, Cheng J W, Liu P Y, Li C D, Sun Y R, Huang Y, Ren Z A, and Chen G F 2024 *Phys. Rev. B* **109** 125112
[58] Hu J F, Ernst B, Tu S, Kuveždić M, Hamzić A, Tafra E, Basletić M, Zhang Y G, Markou A, Felser C, Fert A, Zhao W S, Ansermet J P, and Yu H M 2018 *Phys. Rev. Appl.* **10** 044037
[59] Ikhlas M, Tomita T, Koretsune T, Suzuki M T, Nishio-Hamane D, Arita R, Otani Y, and Nakatsuji S 2017 *Nat. Phys.* **13** 1085